Combustion Modeling Study for GCH4/GO2 Multi-element Combustion Chamber

By Y. Daimon†, H. Terashima‡, D. Muto†, H. Tani†, H. Negishi†, AND O. J. Haidn¶

Japan Aerospace Exploration Agency, 2-1-1 Sengen, Tsukuba, Ibaraki, Japan

A comparison of numerical predictions for gaseous oxygen gaseous methane (GCH_4) / gaseous oxygen (GOX) single- and multi-element rocket combustion chambers is conducted. The simulation results are validated using static firing tests performed by Technical University of Munich. Those results accurately predict the pressure and wall heat flux profiles on a cylindrical part of the combustion chambers for the hot firing test. The differences between the single- and multi-element combustion chambers are flame-flame interaction in the outer-row injectors. The effects of the flame-flame interaction are observed in the GOX core lengths, velocity fields, and unmixedness in the flowfields. The simulation has an issue in predicting wall heat flux on the nozzle part. In the multi-element combustion chamber, the prediction error is 30 %. Two kinds of tests are conducted to understand this error. First, 2D axisymmetric combustion simulation of the thrust chamber without injectors is performed with fully combusted gas. Second, an empirical correlation (i.e., Bartz's equation) is applied for this chamber. Both results show underestimated wall heat flux on the nozzle part for the experimental data.

1. Introduction

Oxygen/methane is a very attractive propellant combination in the space propulsion field due to their ease in handling, low operational costs, and high specific impulse. Although the liquid oxygen/methane propellant combination is an attractive option, only a limited amount of experimental data at relevant combustion chamber conditions is available, and a critical gap is present in the knowledge of detailed heat transfer characteristics and injector technology. Improving our knowledge about the heat transfer processes and cooling methods in the combustion chamber is crucial to develop high-performance liquid rocket engines.

Within this framework, experimental test campaigns were performed at the Technical University of Munich (TUM) on gaseous methane (GCH_4)/gaseous oxygen (GOX) shear coaxial single- [1, 2] and multi-element injectors [3], and wall heat transfer characteristics were discussed. In Summer Program 2015 of SFB/TRR 40, steady-state simulation for Reynolds-averaged Navier-Stokes simulations (RANS) for a single-element with a square chamber [2] was used to reproduce the combustion pressure and wall heat flux distributions, and the results were compared with the experimental data [4]. In addition, the several physical models have been tested, and these characteristics have been revealed. In this study, the same approach as used in the previous work [4] was applied

† Research and Development Directorate, Japan Aerospace Exploration Agency
‡ Faculty of Engineering, Hokkaido University
¶ Department of Mechanical Engineering, Technical University of Munich

to single- [1] and multi-element with a round chamber [3]. The differences in flowfields between the single- and multi-element combustion chambers were discussed. The comparison is very reasonable as the single- and multi-element combustion chambers designed by TUM had identical basic configurations in terms of injector configurations, contraction ratio, and injector-wall distance.

2. Reference experiment

All test campaigns described in this study were performed at the Institute of Flight Propulsion's facility at TUM [1, 3]. This section describes the computational objects and conditions.

Figure 1 shows the test configuration of the multi-element injector combustion chamber [3]. The seven-element combustion chamber with an inner diameter of 30 mm and a contraction ratio of 2.5 is designed to understand flame-flame interaction. In order to easily scale the chamber with the injector dimensions, the distance between the injectors as well as the injector-wall-distance are kept constant and equal to half of the injector diameter, resulting in a pattern of seven injector elements. The combustion chamber is comprised of four cylindrical water-cooled chamber segments, one long and three short segments, and a nozzle segment for a total length of 341+42 mm. The wall heat flux profile along the combustion chamber axis was calculated as integral value of water heat up in the cooling channels.

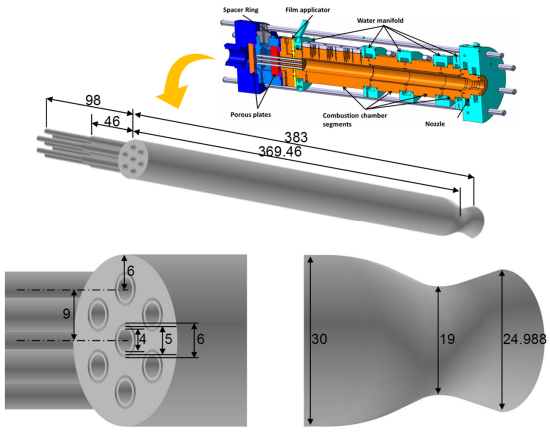

FIGURE 1. Configuration of the multi-element combustion chambers.

Figure 2 shows the configuration of the single-element injector combustion chamber [1]. The combustion chamber is 12 mm in diameter and has a contraction ratio of 2.5. The thrust chamber length up to the throat is 303 mm. In order to compare this chamber with the multi-element combustion chamber, the injector-wall-distance is equal to half of the injector diameter, and thus the same distance in the multi-element combustion chamber. The single-element combustion chamber also has the same the injector configuration as that of the multi-element combustion chamber. Therefore, the multi- and single-element can be compared to understand flame-flame interaction. To determine the temperature field, the chamber segments are equipped with type T thermocouples

spring-mounted in the chamber wall. The wall heat flux and surface temperature were reconstructed using the thermocouple temperature.

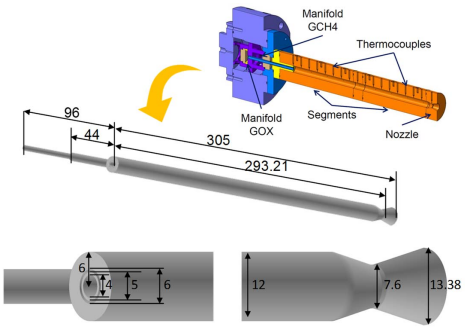

FIGURE 2. Configuration of the single-element combustion chamber.

Table 1 lists the conditions for the test campaigns of the single- and multi-element combustion chambers [1, 3]. The mass flow rate per element in the multi-element combustion chamber is lower than that in the single-element combustion chamber. TUM arranged the mass flow rate to match the wall heat flux level between the single- and multi-element combustion chambers. Generally, the wall heat flux level largely depends on the combustion pressure and contraction ratio. As shown in Figs. 1 and 2, the contraction ratios between the single- and multi-element combustion chambers were identical. The chamber diameter was determined in consideration of the injector dimensions and injector-wall-distance. The throat diameter was derived from the chamber diameter and contraction ratio. Therefore, the mass flow rate was calculated from the throat diameter to match the combustion pressure between single- and multi-element chambers.

TABLE 1. Test conditions.

	Single	Multi
O/F	2.64	2.65
Mass flow oxid, kg/s	0.0351	0.211 (0.0301 per single)
Mass flow fuel, kg/s	0.0133	0.08 (0.0114 per single)
Temp, oxid, K	275.1	259.4
Temp, fuel, K	269.4	237.6
Pressure, MPa	1.95	1.91

3. Computational Setup

3.1. *Numerical Method*

The numerical methods used in this study were the same as used in the last summer program [4]. The numerical simulations were performed using the density-based solver

CRUNCH CFD developed by Combustion Research and Flow Technology (CRAFT Tech) [5]. CRUNCH CFD is an unstructured/multi-element flow solver based on a cell-vertex method [5,6]. The governing equations are three-dimensional (3D) compressible Favre-averaged Navier-Stokes equations. Inviscid fluxes are calculated using a second-order linear reconstruction procedure based on a total variable diminishing scheme. Viscous fluxes are computed by estimating gradients at cell faces. Standard high Reynolds number $k-\epsilon$ turbulence models with two layer near-wall treatment [7] are used. For time integration, an implicit solution procedure is employed, allowing for Gauss-Seidel or generalized minimal residual solver options with a preconditioning matrix using a distance-one neighbor bandwidth [6]. A laminar finite rate model with a skeletal chemical reaction set of CH_4/O_2 proposed by DLR [8] is used as the combustion model. This model includes 21 species and 97 chemical reactions.

Figure 3 shows the computational domain with the boundary conditions of (a) single- and (b) multi-element combustion chambers. For the single-element combustion chamber, two-dimensional axi-symmetric simulation was performed. For the multi-element combustion chamber, a symmetry condition was assumed in the circumferential direction, with only 30 degrees of the chamber being simulated. For the boundary conditions in both cases, the supersonic outflow condition is imposed on the nozzle outlet, and the mass flow rate and static temperature of CH_4/O_2 are specified at the inlet boundaries for each fluid, as listed in Table 1, and thus the chamber pressure obtained by the computation can be compared with the experimental value. A no-slip and isothermal wall with temperature distribution estimated from the experiment is applied to the combustion chamber wall. The temperature of the last part of the combustion chamber was used as the nozzle wall temperature because the nozzle wall temperature was not measured in the experiment. For the other walls, no-slip and adiabatic conditions are imposed.

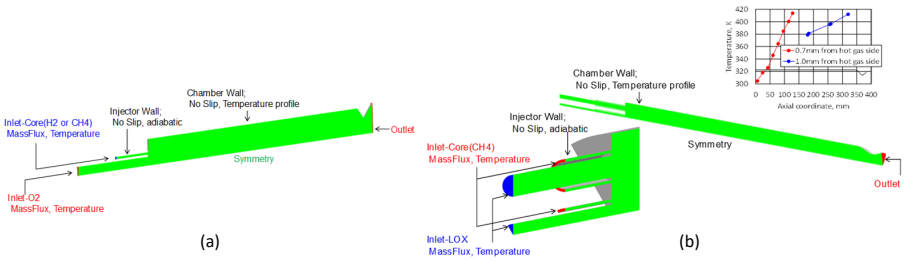

FIGURE 3. Computational domain and boundary conditions of (a) single- and (b) multi-element combustion chamber.

3.2. *Grid Resolution Study*

A grid resolution study was conducted using three kinds of grid distributions. Figure 4 shows the computational grid used for base resolution of the multi-element combustion chamber, which includes the vicinity of the injector, middle of the combustion chamber, and the nozzle. The mesh is clustered around the shear layer between the flow of CH_4 and O_2, and the thrust wall to reproduce the diffusion flames and thermal boundary layer on the wall. There are approximately 4.7 million computational grid points, in which y^+ of the near-wall grid is about 0.1 along the entire region, and 41 grid points are used on the GOX post for the base grid.

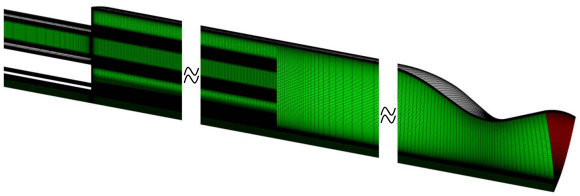

FIGURE 4. Computational grid of multi-element combustion chamber.

Figure 5 shows the grid distributions of (a) coarse, (b) base, and (c) fine grids on the faceplate of the multi-element combustion chamber. The numbers of grid nodes for the coarse, base, and fine grids on the circular arc are 21, 31, and 47 nodes, respectively. The numbers of grid nodes of the coarse, base, and fine grids on the GOX post are 27, 41, and 61 nodes, respectively. As a result, the total grid nodes for the coarse, base, and fine grid are 1.2, 4.7, and 10.2 million, respectively.

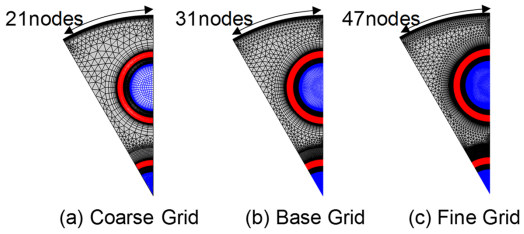

FIGURE 5. Computational grid of multi-element combustion chamber.

Figure 6 shows the simulated temperature distributions using the (a) coarse, (b) base, and (c) fine grids. The high temperature region that corresponds to the diffusion flame is gradually extended. Conversely, the low temperature region that corresponds to the GOX core is gradually narrowed. The GOX core lengths of all grids are almost identical.

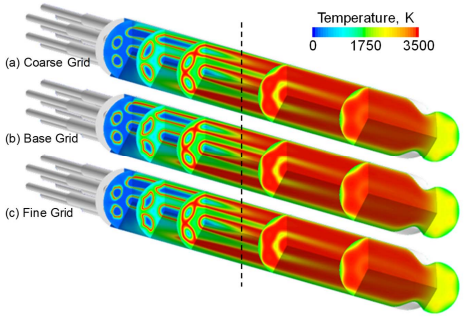

FIGURE 6. Temperature distributions of multi-element combustion chamber using the (a) coarse, (b) base, and (c) fine grid.

Figure 7 shows the (a) heat flux distributions and (b) wall pressure profiles obtained with different grid resolutions. Those profiles in all cases were almost identical. Therefore, the base grid was used for the discussion below. The grid distributions of the single-

element combustion chamber are based on the base grid of the multi-element combustion chamber. There are 41 grid nodes on the GOX post, and y^+ of the near-wall grid is about 0.1 along the entire region. And the single-element combustion chamber has approximately 0.11 million total computational grid points.

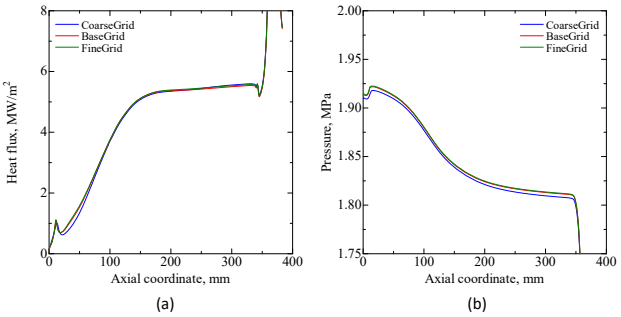

FIGURE 7. (a) Wall heat flux and (b) wall pressure profiles using the coarse, base, and fine grid.

4. Results and Discussion

The validation of pressure and wall heat flux profiles in the single- and multi-element combustion chambers are described at the beginning. Then differences in the computed flow fields between the single- and multi-element combustion chambers are discussed. In particular, the physical phenomena of flame-flame interaction in the multi-element combustion chamber are described using the flow fields. Finally, the accuracy of the predicted wall heat flux on the nozzle part is discussed using a simple simulation and an empirical correlation.

4.1. *Validations*

Figure 8 shows the wall pressure distributions of the experimental data and simulation results in the single- and multi-element combustion chambers. The experimental data for both the single- and multi-element combustion chambers showed a small rise from points 1 and 2 near the faceplate, followed by a gradual decrease. The simulation results could reproduce these characteristics of the pressure profiles. The prediction errors of combustion pressure at the wall between the simulation results and experimental data were +2.4% and +1.6%, respectively.

Figure 9 shows the wall heat flux distributions of the experimental data and simulation results for the (a) single- and (b) multi-element combustion chambers. The experimental data for the single-element combustion chamber was obtained by the inversed method of measured wall temperature. The simulation results agreed well with the experimental data overall. The experimental data had some spikes of around 180 mm. This oscillation occurred due to the initial heat shock caused by ignition. Therefore, the discrepancy in the wall heat flux profiles between the experimental data and simulation results was only seen near the faceplate. The experimental data for the multi-element combustion chamber was obtained by the calorimetric method using the water-cooled chamber. Therefore, the heat flux profile was calculated as an integral value of water heat up in the cooling channels. The simulation results for the multi-element combustion chamber were also integrated at the same position for each water-cooled segment. The simulated

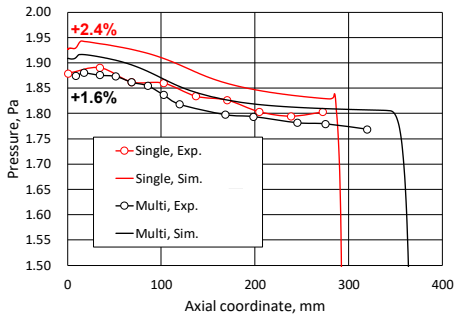

FIGURE 8. Comparison of the wall pressure profiles between experimental data and simulation results of single- and mulit-element combustion chamber.

total heat load of the cylindrical part was only 2.7% lower than in the experimental data. However, the simulated heat load of the nozzle part was significantly lower (30%) than in the experimental data. This discrepancy is discussed in Section 4.3.

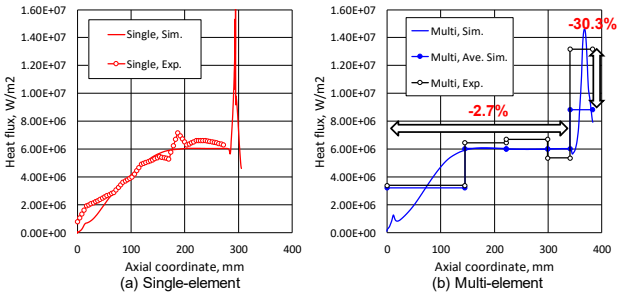

FIGURE 9. Comparison of the heat flux distributions between experimental data and simulation results of (a) single- and (b) mulit-element combustion chamber.

4.2. *Comparison between single- and multi-element combustion chambers*

Figure 10 shows a comparison of wall heat flux between the single- and multi-element combustion chambers relative to the (a) experimental data and (b) simulation results. The experimental data of the single-element chamber was integrated at the same position for the first and second water-cooled segments for a comparison with the multi-element combustion chamber. The integrated heat load in the first and second segments of the single-element combustion chamber is slightly lower than that of the multi-element combustion chamber. This characteristic could be observed in the simulated results at $70 < x < 200$ mm as shown in Fig. 10b. These regions corresponds to the flame developing zones in the combustion chambers.

Figure 11 shows the temperature flowfields of the (a) single- and (b) mulit-element combustion chambers to understand the wall heat flux differences at $70 < x < 200$ mm. The temperature flowfields between the single- and multi-element combustion chambers had the same configuration, such as the low temperature region at the corner of the combustion chamber, the GOX core, diffusion flame, and thermal boundary layer on the chamber wall. Quantitatively, the GOX core length of the single-element combustion chamber was longer than that of the multi-element combustion chamber. Therefore, in

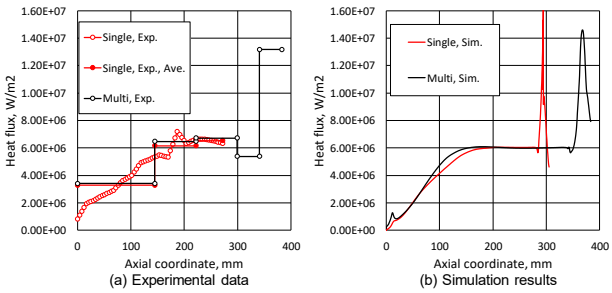

FIGURE 10. Comparison of wall heat flux between single- and multi-element combustion chamber of (a) experimental data and (b) simulation results.

order to understand the differences between the single- and multi-element combustion chambers, heat convection to the wall and flame-flame interaction due to the effect of the GOX core length should be discussed.

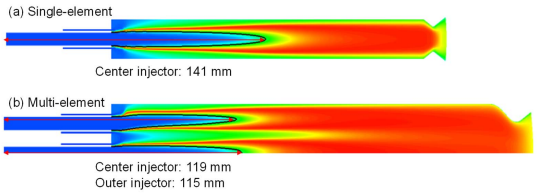

FIGURE 11. Comparison of the temperature distribution of single- and multi-element combustion chamber of (a) experimental data and (b) simulation results.

At first, the effect of the wall boundary condition was examined because the ratio between the surface area and combustion chamber volume differs between the single- and multi-element combustion chambers. Figure 12 shows the temperature distributions and pressure profiles in order to compare the cases of iso-thermal and adiabatic walls. The GOX core lengths were almost identical regardless of the boundary condition. However, the pressure profile with the adiabatic wall condition was at a level higher than that with the iso-thermal wall condition because the low temperature wall reduces energy in the combustion chamber. It was found that heat convection to the chamber wall did not affect the GOX core length.

Flame interaction was then discussed. Figure 13 shows the temperature distribution in six cross sections (at 10, 25, 50, 75, 100 and 125 mm) for the single- and multi-element combustion chambers. The outer-row flame shapes were characteristic of the multi-element combustion chamber. Flame-wall interaction induced longitudinal vortices near the wall and generated flames of the elliptical shape in the outer row. This flame-flame interaction began around x = 75 mm in the outer-row flames. At x = 100 mm, the outer flames merged together. The position of flame-flame interaction corresponded to the wall heat flux distributions. As shown in Fig. 10, the heat flux differences began from x = 75 mm.

Figure 14 shows the axial velocity distributions in the cross section for the single- and multi-element combustion chambers. At x = 75 mm where flame-flame interaction began in the outer-low flames, a high velocity region appeared near the flame-flame

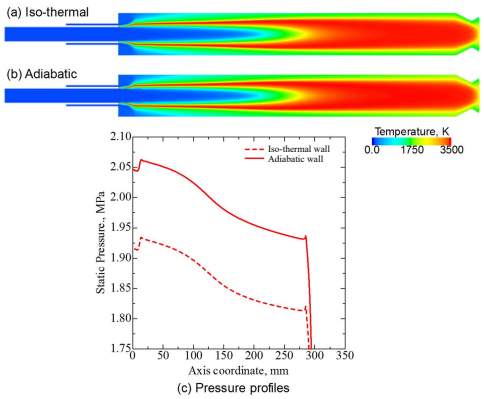

FIGURE 12. Comparison of (a) (b) temperature distributions and (c) pressure profiles between iso-thermal and adiabatic wall.

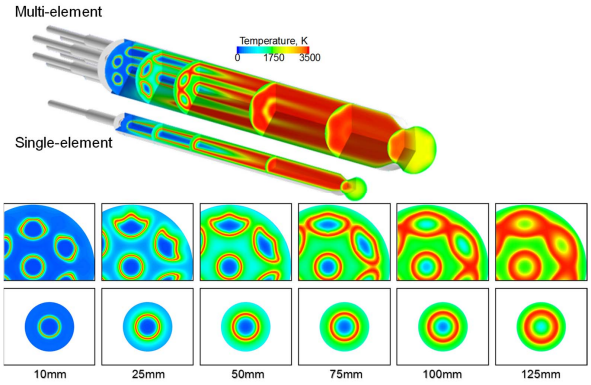

FIGURE 13. Comparison of temperature distributions in the cross sections between single- and multi-element combustion chambers.

interaction. At x = 100 mm, the differences in axial velocity distribution between the single- and multi-element combustion chambers were observed more clearly. This high velocity induced the strong shear layers and promoted mixing.

Figure 15 shows the unmixedness for the single- and multi-element combustion chambers in order to understand the status of mixing. The unmixedness for the multi-element combustion chamber was better than that for the single-element combustion chamber from x = 70 to 200 mm. This difference in unmixedness corresponded to the difference in wall heat flux between the single- and multi-injection combustion chambers as shown in Fig. 10. From the discussions of wall boundary conditions and flame-flame interaction, the mixing and combustion between the outer-row injectors were found to be enhanced with flame-flame interaction in the multi-element combustion chamber.

4.3. *Prediction accuracy of wall heat flux on nozzle part in multi-element combustion chamber*

This section discusses the prediction accuracy of wall heat flux on the nozzle part in the multi-element combustion chamber. As shown in Fig. 9, the error of simulation results

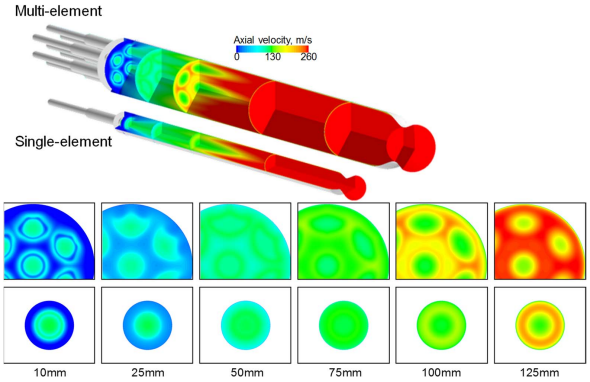

FIGURE 14. Comparison of axial velocity distributions in the cross sections between single- and multi-element combustion chambers.

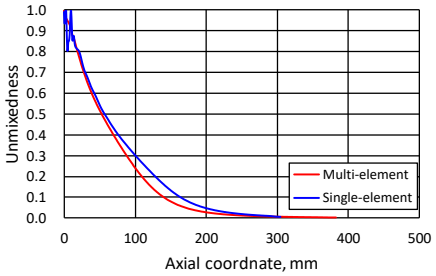

FIGURE 15. Unmixedness profiles of single- and multi-element combustion chambers.

for the wall heat flux on the nozzle part was about –30%. We conducted two kinds of tests to understand this error. In Fig. 13, the thermal boundary layer had non-uniformity distribution in the circumferential direction at the throat. Therefore, the mixing could be insufficient. As the first test, 2D axi-symmetric combustion simulation of the thrust chamber without injectors was performed with fully combusted gas, and calculated using NASA CEA code [9]. Its combustion temperature was 3270 K. This simulation using fully combusted gas did not include any effect of the injector positions. In other words, the results indicate the maximum wall heat flux in the simulation. As the second test, Bartz's equation [10] was applied for this chamber. Bartz's equation can take into account Mach number effect but not the rate of chemical reaction. The reaction time in the nozzle part can ignore using Bartz's equation. We then compared the simulation results and Bartz's equation data.

Figure 16 shows the temperature distributions and circumferential averaged wall heat flux profiles for the 2D axisymmetric simulation results without injectors and 3D simulation results with injectors. The thermal boundary layer was developed on the chamber wall. Fig. 16c includes the experimental data, 2D axisymmetric simulation results without injectors, and 3D simulation results with injectors. The simulation results were integrated in each water-cooled segment. The wall heat flux for 2D axisymmetric simulation with-

out injectors was higher than that for 3D simulation with injectors. However, the wall heat flux on the nozzle for 2D axisymmetric simulation without injectors was still significantly lower than for the experimental data.

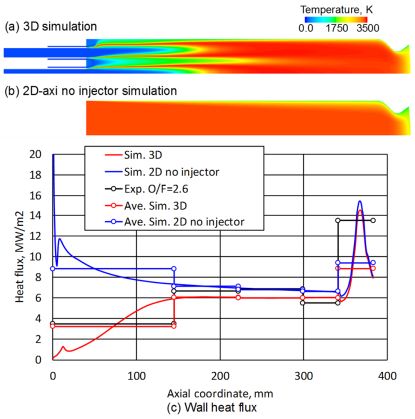

FIGURE 16. Temperature distributions and wall heat flux profiles of three-dimensional and two-dimensional without injectors simulations.

Figure 17 shows the wall heat flux for the experimental data, 3D simulation results, and Bartz's equation results with empirical coefficients 0.2 and 0.29. It also shows the simulation results and Bartz's equation results integrated at the water-cooled segment. The empirical coefficient 0.2 was selected to fit the wall heat flux on the cylindrical part for both the 3D simulation results and the experimental data. As a result, the level of wall heat flux on the nozzle part for the 3D simulation results was almost the same as that for the Bartz's equation with 0.2. The empirical coefficient 0.29 was selected because integrated wall heat flux on the nozzle part obtained by Bartz's equation adopted the experimental data. As a result, the level of wall heat flux on the cylindrical part derived by Bartz's equation was higher than that in experimental data.

Responding to the results of the above two tests, we figured out that the wall heat flux on the nozzle part in the experimental data was too high under these boundary conditions. As mentioned in Sec. 3.1, the wall temperature of the nozzle part was not measured in the experimental data. In order to reveal this discrepancy in wall heat flux and the effect of boundary conditions on the thrust chamber wall, a conjugated simulation between hot gas and water cooling will be performed in future work.

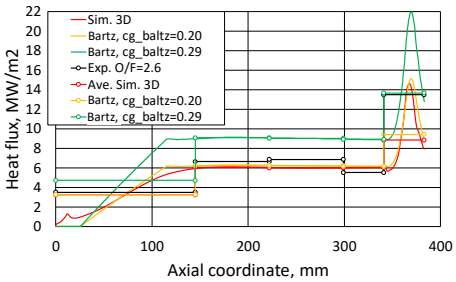

FIGURE 17. Heat flux profiles derived by three-dimensional simulation results and Bartz's equation.

5. Conclusions

3D RANS simulations were performed for the static firing test of GCH_4/GOX coaxial single- and multi-element injectors with a round chamber that were performed at TUM. The computed results were validated using the pressure profile and circumferentially averaged heat flux distributions, and showed good agreement with the experimental data in the cylindrical part overall. Specifically, the combustion pressures in the simulation results of single- and multi-element combustion chambers were 2.4% and 1.6%, respectively, and thus higher than those in the experimental data. The simulation results of wall heat flux in the cylindrical part for both combustion chambers slightly underestimated the value near the faceplate. At the flame developing zone, the flame-flame interaction in the outer-row injectors of the multi-element combustion chamber were observed. The effect of the flame-flame interaction appeared in the wall heat flux, GOX core length, velocity distributions, and unmixedness.

Finally, the prediction accuracy of wall heat flux on the nozzle wall in the multi-element combustion chamber was discussed. The error of integrated wall heat flux in the three-dimensional simulation results with injectors was –30% on the nozzle part. Two kinds of tests were conducted to find the cause of this error. As a first test, two-dimensional axi-symmetric simulation without injectors was performed. Instead of the multi-element injectors, fully combusted gas was imposed at the inlet boundary. The integrated heat flux in the two-dimensional simulation was lower than that in the experimental data. Next, Bartz's equation was applied for the multi-element combustion chamber. An empirical coefficient could not be found to match the level of wall heat flux in both the cylindrical and nozzle parts. In particular, empirical coefficient 0.2, which was selected to match the wall heat flux on the cylindrical part for the three-dimensional simulation results and the experimental data, could not recreate the experimental data on the nozzle part. Responding to these results, we concluded that wall heat flux on the nozzle part in the experimental data was too high under these boundary conditions.

Acknowledgments

Financial support has been provided by the German Research Foundation (Deutsche Forschungsgemeinschaft – DFG) in the framework of the Sonderforschungsbereich Transregio 40. All the simulations of JAXA carried out in this study were performed on the JAXA Supercomputer System (JSS).

References

[1] ROTH, C., SILVESTRI, S., PERAKIS, N. AND HAIDN, O. (2017). Experimental and numerical investigation of flow and combustion in a single element rocket combustor using GH2/GOX and GCH4/GOX as propellants. In: *31st International Symposium on Space Technology and Science*.

[2] SILVESTRI, S., PALMA, C.M., HAIDN, O. AND KNAB, O. (2015). Comparison of single element rocket combustion chambers with round and square cross sections. In: *6th European conference for aeronautics and space sciences*.

[3] SILVESTRI, S., KIRCHBERGER, C., SCHLIEBEN, G., PALMA, C.M. AND HAIDN, O. (2017). Experimental and numerical investigation of a multi-injector GOX-GCH4 combustion chamber. In: *31st International Symposium on Space Technology and Science*.

[4] DAIMON, Y., TERASHIMA, H., NEGISHI, H. AND HAIDN, O. (2015). Combustion modeling study for a GCH4/GOX single element combustion chamber: Steady state simulation and validations. In: *Proceedings of the SFBTRR40 Summer Program 2015*. 141–150.

[5] HOSANGADI, A., LEE, R.A., YORK, B.J., SINHA, N. AND DASH, S.M. (1996). Upwind unstructured scheme for three-dimensional combustion flows. *Journal of Propulsion and Power*, **12**(3), 494–503.

[6] HOSANGADI, A., LEE, R.A., CAVALLO, P., SINHA, N. AND YORK, B.J. (1998). Hybrid, viscous, unstructured mesh solver for propulsive applications. In: *34th AIAA/ASME/SAE/ASEE Joint Propulsion Conference and Exhibit, AIAA Paper 1998-3153*.

[7] WOLFSHTEIN, M. (1969). The velocity and temperature distribution in one-dimensional flow with turbulence augmentation and pressure gradient. *Int J. Heat and Mass Transfer*, **12**, 301–318.

[8] SLAVINSKAYA, N. (2015). Methane skeltal mechanism for space propulsion applications. In: *5th International Workshop on Model Reduction in Reacting Flows*.

[9] GORDON, S. AND MCBRIDE, B.J. (1994). Computer program for calculation of complex chemical equilibrium compositions and applications. In: *NASA Reference Publication 1311*.

[10] BARTZ, D. (1957). A simple equation for rapid estimation of rocket nozzle convective heat transfer coefficients. *Jet Propulsion*, **27**(1), 49–51.